Complex-Valued Analysis of Arterial Spin Labeling–Based Functional Magnetic Resonance Imaging Signals

Luis Hernandez-Garcia,[1*] Alberto L. Vazquez,[2] and Daniel B. Rowe[3]

Cerebral blood flow-dependent phase differences between tagged and control arterial spin labeling images are reported. A biophysical model is presented to explain the vascular origin of this difference. Arterial spin labeling data indicated that the phase difference is largest when the arterial component of the signals is preserved but is greatly reduced as the arterial contribution is suppressed by postinversion delays or flow-crushing gradients. Arterial vasculature imaging by saturation data of activation and hypercapnia conditions showed increases in phase accompanying blood flow increases.

An arterial spin labeling functional magnetic resonance imaging study yielded significant activation by magnitude-only, phase-only, and complex analyses when preserving the whole arterial spin labeling signal. After suppression of the arterial signal by postinversion delays, magnitude-only and complex models yielded similar activation levels, but the phase-only model detected nearly no activation. When flow crushers were used for arterial suppression, magnitude-only activation was slightly lower and fluctuations in phase were dramatically higher than when postinversion delays were used.

Although the complex analysis performed did not improve detection, a simulation study indicated that the complex-valued activation model exhibits combined magnitude and phase detection power and thus maximizes sensitivity under ideal conditions. This suggests that, as arterial spin labeling imaging and image correction methods develop, the complex-valued detection model may become helpful in signal detection. Magn Reson Med 62:1597–1608, 2009. © 2009 Wiley-Liss, Inc.

Key words: complex-valued; phase; ASL; FMRI analysis; perfusion; cerebral blood flow

Until recently, functional magnetic resonance imaging (FMRI) data analysis was concerned only with the magnitude of the image time courses, although the data are intrinsically complex valued. Indeed, most MR images are reconstructed from complex-valued signals collected by quadrature detectors and most reconstruction techniques yield complex-valued images. Yet the phase information is routinely discarded, retaining only the magnitude images (1). Recently, complex-valued FMRI activation models with combined magnitude and phase (MP) detection have been developed by Rowe and Logan (1) and Rowe (2) for blood oxygen level dependent (BOLD) contrast FMRI time series (1,2). Although our mechanism is not BOLD based, we aim to take advantage of these models for arterial spin labeling (ASL) FMRI. The complex-valued models are designed to detect task-related phase changes (TRPCs) in addition to task related magnitude changes. The complex model's ability to detect TRPCs increases the possible circumstances under which activation is detected for given signal-to-noise ratio (SNR) and contrast-to-noise ratio (CNR). Changes in the signal's phase were described by Menon (3), who put forth a model explaining how the physiologic changes that give rise to the BOLD effect manifest themselves in the magnitude and the phase of the signal, particularly in areas of larger venous vasculature. This effect was utilized to reduce the contribution of the further downstream venous vasculature to the magnitude activation (4). ASL time series are typically used as indicators of perfusion (a real-valued quantity), but ASL time series can be designed to be BOLD weighted as well (5-7).

The SNR and CNR in ASL techniques are inherently low (8-11), making ASL-based FMRI more challenging than BOLD-based FMRI. For example, Perthen et al. (10) reports SNR maps in the range of one to two for ASL and more than 100 for BOLD data. Yang et al. (11) report t-scores of approximately 5 for ASL data, whereas BOLD data produce t-scores greater than 10, reflecting the CNR difference. It is therefore imperative that statistical analyses of ASL data be as efficient and sensitive as possible. Typical ASL analysis (ordinary least squares analysis of the subtracted magnitude data) results in reduced estimation efficiency (6) and "wastes" information by using only the magnitude of the signals because potentially valuable phase information is routinely discarded. Complex-valued analysis techniques should also benefit regression analysis of ASL data. Furthermore, the presence of the inversion-labeled ASL data can also induce changes in the phase of the labeled images, also called tagged images, relative to the control images, as we discuss below in greater detail.

In this article, we examine the biophysical basis for phase changes in the ASL signal (independent of the BOLD effect-related phase changes) and develop an analysis approach for ASL time series that includes generalized least-squares analysis of the complex-valued, undifferenced ASL data. This analysis scheme models the changes in perfusion and BOLD contrast as complex-valued (MP) quantities. The model and techniques in this work are demonstrated on continuous ASL data but are equally applicable to pulsed ASL. Complex-valued analysis of ASL data could potentially increase the sensitivity and specificity of functional studies and also help identify vascular sources of noise.

[1]Functional MRI Laboratory, University of Michigan, Ann Arbor, Michigan
[2]Department of Radiology, University of Pittsburgh, Pittsburgh, Pennsylvania
[3]Department of Biophysics, Medical College of Wisconsin, Milwaukee, Wisconsin

Correspondence to: Luis Hernandez-Garcia, Ph.D., FMRI Laboratory, 2360 Bonisteel Blvd, Ann Arbor, MI 48109-2108. E-mail: hernan@umich.edu
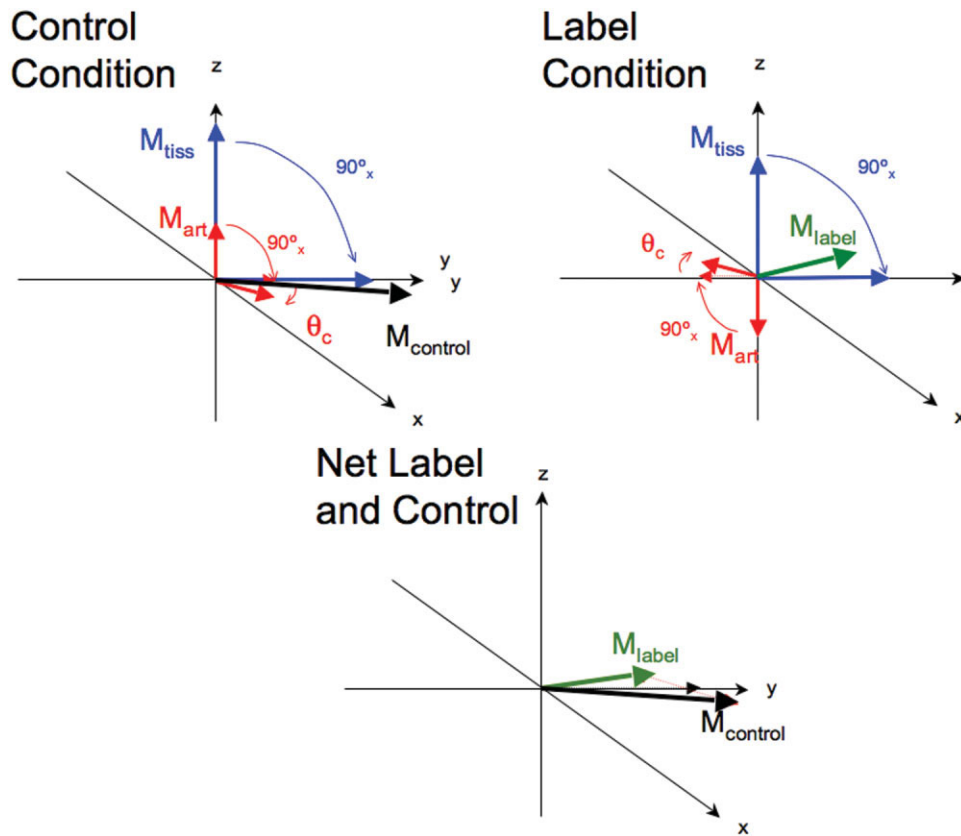
FIG. 1. Simple cartoon (not drawn to scale) illustrating the sources of magnetization and their phase gain during the acquisition segment of an ASL experiment. Blue arrows indicate the magnetization caused by the tissue spins, and red arrows indicate the magnetization from the arterial sources. The net magnetization vectors under control and labeled conditions are shown in black and green, respectively. Note that the tissue magnetization vector is shortened as the tagged blood exchanges into the tissue.

Vector Model of ASL Signals

Pairs of images are acquired in a typical ASL experiment: One is preceded by a tagging period, in which the inflowing arterial spins are inverted (tagged), and a second control image without the inversion label (control). Fig. 1 depicts the magnetization vectors for the tissue and blood pools under labeling and control conditions. Within the voxel, a fraction of the spins are in the tissue and their movement is governed by random diffusion. Indistinguishable from tissue is also the isotropic capillary perfusion, although it occurs at a faster rate. A smaller fraction of the spins is in the vasculature and its motion is governed by anisotropic, coherent flow (3,12).

In the control images, the coherently moving vascular spins acquire some net phase, ϕ, that does not get refocused by the imaging pulse sequence. This net phase gain is due to motion in the presence of the imaging magnetic field gradients and has been studied extensively both as a source of artifacts (13) and contrast to identify vasculature (14). The net phase gain of the incoherently moving spins (i.e., those of the tissue and capillaries), on the other hand, is zero because of their isotropic motion.

In the tagged case, the arterial magnetization is inverted by the labeling RF pulses and gradually relaxes back along the z-axis toward its equilibrium state. If the arrival time is short enough, the incoming arterial magnetization is still

in the negative longitudinal axis at the time the imaging pulses of the imaging sequence are applied. The magnetization vector is tipped onto the transverse plane by the imaging RF pulses, but 180° from the tipped location of the control case (for a visual example of this effect, please see Fig. 3 of Hernandez-Garcia et al. (15)). The net phase gain of the vascular spins is then ϕ + 180. If the arrival time is sufficiently long for the labeled spins to have relaxed past the null point ($M_z = 0$) but not yet be fully relaxed, the net phase from the coherent compartment is the same as in the control case. The magnitude of the vascular magnetization vector, however, is shorter than in the control case.

In both control and tagged cases, the tissue's net magnetization vector does not acquire any net phase because the movement of the spins due to perfusion and diffusion is mostly isotropic. Hence, when there is a significant arterial contribution in the ASL signal, the inversion label should cause the net (vascular plus tissue) magnetization vector to change in both MP. If there is not a significant arterial contribution to the signal, only the magnitude of the signal is expected to change.

The phase gained by the coherently flowing vascular spins can vary widely between 0 and 360 degrees, depending on their velocity and the gradients used in the acquisition sequence. However, to estimate the upper bound for the size of this effect, let us assume the most noticeable

scenario to be expected in physiologic conditions: a 90-degree phase gain in arterial vasculature relative to tissue, 5% of a voxel's volume to be occupied by arterioles and 15% to be occupied by large arteries, and perfect inversion labels. This would produce a phase difference of 6.8 degrees between control and tagged images because of the arterioles and 22 degrees if the signal from large arteries is also included (not suppressed). It should be noted that the observed effects reported below are much smaller than this theoretic upper bound, but still observable.

It should be noted that in the Menon (3) model for the BOLD effect, the phase differences are produced by local resonance frequency shifts in venous areas because of increases in the amount of oxygenated blood. The BOLD phase differences are a function of the T_2^* weighting of the imaging sequence and can be minimized by spin echo imaging. Although Menon's model focused on the venous contribution to the MR signal and its phase changes associated with neuronal activation, the vector model in this article is mainly concerned with the arterial and arteriolar contribution because no significant amount of the inversion label reaches the veins, and BOLD effects are assumed to be significantly diminished by spin-echo acquisition. A complete model for T_2^*-weighted ASL data can be built by including both arterial and venous contributions to the phase separately.

In this article, we measure the phase contributions of the vascular compartment to the MR signal in ASL data by gradually suppressing their contribution to the perfusion signal by using postinversion delays and diffusion gradient pairs. A significant postlabeling delay allows the labeled signal in blood to reach and exchange into tissue. Diffusion gradient pairs are designed to introduce an intravoxel phase accrual in coherently moving spins along the direction(s) of the gradient(s) that aims to cancel their overall signal, whereas stationary spins accrue no net phase. We also examine the phase content of arterial-only images under rest activation and hypercapnia conditions. We then examine the usefulness of complex-valued analysis for ASL-based FMRI with and without vascular suppression.

METHODS

All scanning protocols were performed with a 3.0 T Signa LX Excite scanner (General Electric, Waukesha, WI) in accordance to the University of Michigan's institutional review board regulations.

Arterial Suppression Study

ASL images were collected from four human subjects. The degree of arterial contribution to the signal was varied in each experiment as follows. ASL imaging was done using the pseudo-continuous arterial spin labeling (CASL) sequence (16,17) (spin-echo spiral acquisition with pulse repetition time = 4000 ms, echo time = 15 ms., slice thickness = 7 mm, field of view = 24 cm, one slice, 96 time frames). The labeling pulses consisted of a train of Hanning window shaped pulses (pulse width = 500 µs, pulse spacing = 290 µs, flip angle 22.5 degrees, net gradient moment = $3 \times 10{-}5$ G/cm/s) applied for 3600 ms. The

experiment was repeated using postinversion delays (18) of 0, 1200 and 1800 ms without any flow crushers. The net tagging time was reduced by the amount of the postinversion delay, accordingly. Similarly, a second set of scans was collected with no postinversion delay but in the presence of a pair of flow crushers (pulse width = 2 ms, separation = 8.8 ms, amplitude = 0, 1, 2 and 4 G/cm). The velocity encoding (VENC) values of this pair were *Inf* (i.e., no crushers), 6.6, and 3.3 cm/s along the Y gradient axis.

All images were reconstructed to yield MP images. Motion parameters were estimated from the magnitude images with MCFLIRT (Oxford University, UK, http://www.fmrib.OX.ac.uk/fsl) to ensure that there was no movement greater than half a voxel shift or 1 degree of rotation. The complex-valued time courses were phase centered by subtracting their angular mean (4) to prevent phase wraps. The images were then pairwise subtracted and the mean and variance of the MP subtractions were computed. *t* Statistics were calculated on the MP differences. Maps of the correlation between MP time courses were computed. Statistical significance of the difference images as well as the correlation images was assessed by the *P* values corresponding to the measured statistics.

Arterial Vasculature Studies Under Activation and Hypercapnia Conditions

An activation study was performed using the arterial vasculature imaging using saturation ASL technique (19). In summary, the arterial vasculature imaging using saturation technique images only the blood signal by completely saturating the background tissue signal (gray matter, white matter, and cerebrospinal fluid) while fresh and fully relaxed blood spins enter the imaging slice. Multiple inversion pulses are then used to maintain the undesired tissue signal nulled while imaging the blood signal after a predetermined time has elapsed (saturation-to-imaging time). This method was determined to be biased to the arterial volume signal. The imaging parameters of the spin-echo spiral acquisition used were field of view = 20 cm, matrix = 40 × 40 (reconstructed to 64 × 64), echo time = 40 ms, saturation-to-imaging time = 800 ms, pulse repetition time = 4000 ms. A visually cued finger-tapping task was used with activation and rest blocks, each of 60 s in duration. During this study, the subject wore a non-rebreathable mask, and 100% air was administered to the subject. A hyperoxic-hypercapnia experiment followed the stimulation experiment. Prior to the start of the acquisition, the administered gas was changed to 100% oxygen and a few minutes were allowed to elapse. A total of 100 images were then acquired, using the same parameters as in the stimulation experiment. The administered gas was switched to 95% oxygen and 5% carbon dioxide 50 s into the acquisition. This gas mixture was supplied for 150 s and then switched back to 100% oxygen. After this experiment finished, the gas mixture was switched back to 100% air.

ASL FMRI Activation Study

ASL images were collected from another human subject by using the same pseudo-CASL sequence described for the
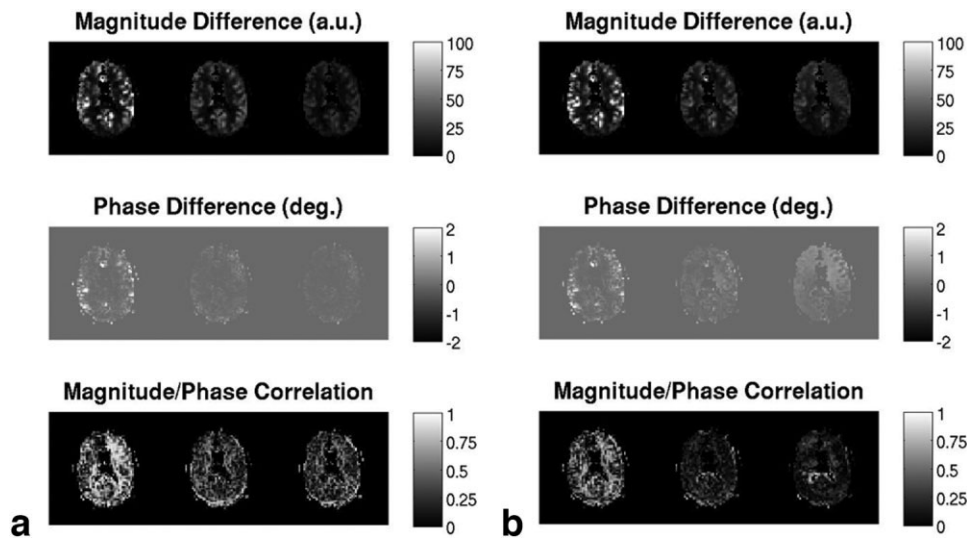
FIG. 2. Arterial contamination removed by (a) two different PID and (b) two different flow-crusher amplitudes. The top row of images shows the mean magnitude subtraction of the time course, the middle row shows the mean phase difference, and the bottom row shows the correlation between magnitude and phase of the unsubtracted data. In (a) the PIDs from left to right were 0, 1200, and 1800 ms. In (b) the VENCs from left to right were *Inf* (i.e., no crushers), 6.6, and 3.3 cm/s along the Y gradient axis.

resting state experiments while they experienced a visual stimulation paradigm (8-Hz flashing checkerboard: six cycles of 50 s rest − 50 s active). Five slices were prescribed, encompassing the visual cortex, and 150 periods were collected. The experiment was performed two additional times with two different methods of arterial signal suppression: a pair of flow-crusher gradients (VENC = 3.3 cm/s), and a postinversion delay of 1200 ms. In this article, we refer to the data collected without arterial suppression or postinversion delays as "whole," those collected with flow crushers as "crush", and those collected with postinversion delays as "PID."

Activation maps were calculated by testing three general linear models for the activation experiments. The first is a linear regression model (linear x with linear y) applied to the magnitude-only (MO) data (20,21) after discarding the phase portion of the data. This model has been shown to be equivalent to a complex-valued model with an unrestricted phase (4). The second is an angular regression model (linear x with angular y) applied to the phase-only (PO) data (22) after discarding the magnitude portion of the data. This model is equivalent to the usual general least squares model for the phase time series when the SNR ratio is high and no phase transitions are present. The third is a complex-valued nonlinear regression model that fully utilizes the MP data (2,23). The details of the models and their underlying distributions are described in the Appendix.

The design matrix utilized for these unsubtracted analyses was composed of a baseline, the BOLD response, an ASL baseline regressor, and an ASL activation regressor, as previously described (9). Together, they make up the columns of the design matrix X while β and γ are regression coefficients in the MP. A contrast C = (0,0,-1,1) was utilized to test hypotheses. For the MO model, parameter estimates and a likelihood ratio–based test statistic are derived from the high SNR normal approximation to Eq.

[A3], considering H_0: Cβ = 0 versus H_1: C$\beta \neq 0$ (4). For the PO model, parameter estimates and a likelihood ratio–based test statistic are derived from the high SNR normal approximation to Eq. [A4], considering H_0: Cγ = 0 versus H_1: C$\gamma \neq 0$ (19). For the complex-valued model, parameter estimates and a likelihood ratio–based test statistic are derived from Eq. [A2], considering H_0: Cβ = 0, Cγ = 0 versus H_1: C$\beta \neq 0$, C$\gamma \neq 0$ (5,6). These hypothesis statements use the traditional abbreviated notation in which Cβ = 0 and Cγ = 0 are also included in the parameter space for the alternative hypotheses. All hypothesis pairs are to detect a difference between tag and control images.

Simulation Study

To examine the detection properties of these three models under ideal conditions, a simulation study was performed. For this simulation, relevant coefficient values were taken to approximate the values from the real data. The SNR = β_0/σ was selected to be 130 and the error standard deviation (SD) to be σ = 1. In our experience, these values represent typical complex FMRI data well. The CNR = Cβ/σ is varied from 0 to 0.75 from left to right in 100 equal steps and TRPC = Cγ is varied from 0 to 21.5 degrees from top to bottom in 100 equal steps. The same design matrix was used as for the real activation study and n = 150. The coefficient values were β = (SNR · σ,5,0, CNR · σ)' in arbitrary units, γ = (30,0.25,0, TRPC)' in degrees. A total of 1500 simulated data sets were generated to make power surfaces.

RESULTS

Arterial Suppression Study

The effects of removing arterial signals from resting ASL images in a representative subject are illustrated in Fig. 2. Fig. 2a shows the results of using postinversion delays for
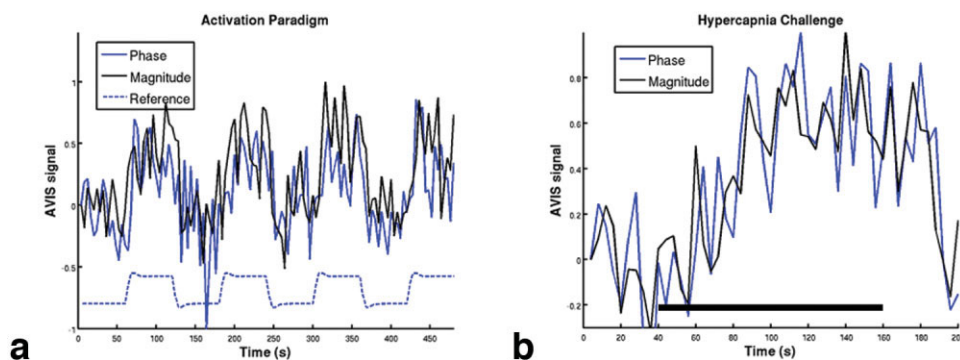
FIG. 3. Magnitude and phase time courses for the arterial vasculature imaging using saturation data extracted from (a) the motor cortex during an activation paradigm (a reference activation function overlaid to indicate activation periods) and (b) a gray matter mask during the CO_2 inhalation experiment (the black bar indicates the timing of the inhalation). [Color figure can be viewed in the online issue, which is available at www.interscience.wiley.com.]

arterial suppression, whereas Fig. 2b shows the results obtained using flow crushers. The resting-state experiments indicated a small phase difference between control and tagged images when no crushers or postinversion delays were employed. The mean value across the brain of the absolute phase difference was 0.3 degrees, with an SD of 0.4 degrees, but it ranged up to 7 degrees in some regions. Maps of the statistical significance of the differences, expressed as $-\log_{10}(p)$ were calculated (data not shown). This difference was much more prominent in voxels dominated by arterial signals, verified by the anatomic images obtained for this study. The first row shows the magnitude difference, whereas the second one shows the phase difference. The bottom row shows the correlation of the unsubtracted MP time courses across the slice. Both methods reduced the arterial contribution to the ASL signal, as evidenced by the reduction in magnitude of the subtraction images (top row). All subjects showed significant differences in MP, and correlations between MP when the arterial signal was preserved. Those effects were reduced by the removal or arterial contribution in all cases.

As expected, introducing arterial suppression techniques reduced the mean gray matter ASL signal (magnitude subtraction of control and tagged images). On average, the inclusion of crushers (VENC of 6.6 and 3.3 cm/s) in the acquisition sequence reduced the magnitude of the ASL subtraction signal by 44.9% and 46.8%, indicating the removal of the signals arising from the major arteries in the field of view. The inclusion of postinversion delays of 1200 and 1800 ms resulted in a magnitude reduction of up to 44.8% and 67.8% respectively.

The difference in phase between control and tagged images was dramatically reduced in both cases as well (middle row). However, as the flow crusher gradient strength was increased, a spatial gradient in the phase difference image could be observed along the direction of the crusher gradient. We attribute this to eddy currents and imperfect gradient stability.

The temporal variance of the pairwise (control minus tag) phase differences (averaged over the tissue) increased dramatically when flow crushers were included (600% and 3100% relative to no crushers). The changes were much smaller when postinversion delays were used to suppress the arterial signal (14%, −16%).

Since both the signal's MP in the arteries are modulated by the same labeling function (i.e., the control-tag scheme), there is a significant degree of correlation between them. The correlation between MP was significantly reduced by the use of postinversion delays and flow-crusher gradients (bottom row), supporting an arterial origin for the correlation. The reduction in correlation was much stronger in the case with diffusion crushers, which increase the phase noise and remove the arterial signal altogether. In the case in which crusher gradients were used, we attribute the reduction in correlation to the drop in SNR at the arteries. In the case of postinversion delays, however, the arterial signal is not destroyed in the unsubtracted time courses. However, the modulation of the arterial signal by the labeling function is no longer present because the labeled blood has been cleared from the arteries during the postinversion delay, and thus the correlation is also reduced.

Arterial Vasculature Studies Under Activation and Hypercapnia Conditions

As discussed elsewhere (19), the arterial vasculature imaging using saturation magnitude data revealed increases in arterial blood flow and volume in the motor cortex during visually cued finger-tapping stimulation. Such magnitude increases were also observed globally during the hypercapnia challenge. In the present analysis, phase increases were also observed along with magnitude changes. Time courses extracted from active regions in the motor activation paradigm can be seen in Fig. 3a. The average phase time course during the CO_2 challenge can be seen in Fig. 3b. Both indicate phase changes closely corresponding to increases in blood flow. These results of arterial vasculature imaging using saturation lend evidence to support that the phase changes of ASL signals stem from arterial signal contributions.

ASL Activation Study

Only one of the five slices was utilized for analysis. Processing prior to statistical analysis entailed quadratic detrending of the MP time series then the first four frequencies ideally filtered. The MO, PO, and MP activations were converted to the $-\log_{10}(p\text{-value})$ scale and thresholded at
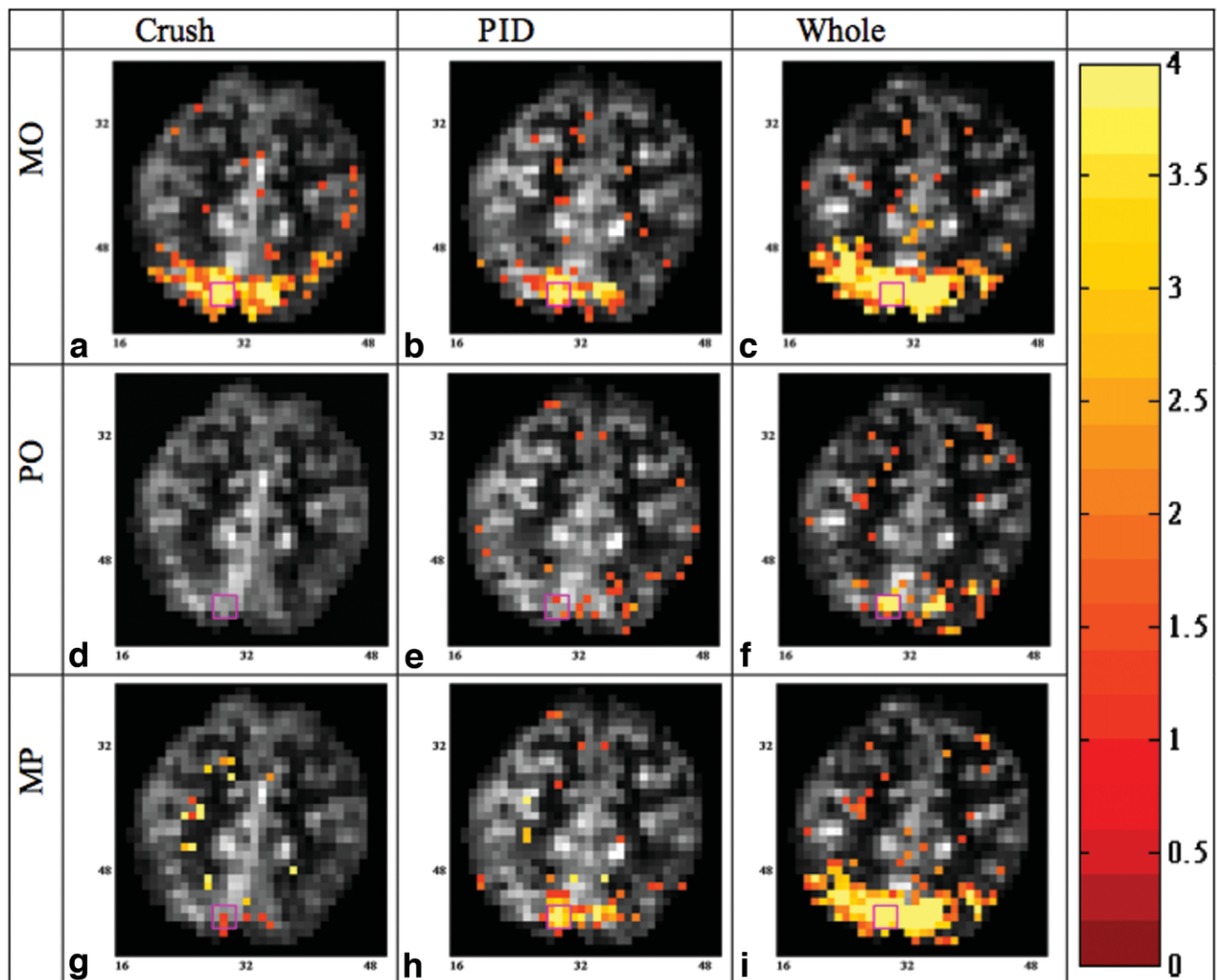
FIG. 4. Activation maps for the three models and three experiments. **a-i:** (a) MO crush,. (b) MO PID, (c) MO whole, (d) PO crush, (e) PO PID, (f) PO whole, (g) MP crush, (h) MP PID, (i) MP whole. All maps are thresholded at $P = 0.05$ or $-\log_{10}(p) = 1.301$.

$P = 0.05$ (21). Activations were superimposed on each scan's magnitude of the complex-valued average of controls minus tags. A region of interest (outlined by the magenta box) within the visual cortex is defined for reference with additional results. The specific location of the box was chosen to include an area that was highly active for the MO analysis in all three data cases. MO activation in the visual cortex was observed using all three sets of data and presented in Figs. 4a-c. Statistically significant activation was detected by the PO model in the visual cortex when the arterial signals were preserved (whole data) in Fig. 4d but not in the crush and PID cases in Figs. 4d and 3e = 4,3. This is indicative that activation-induced perfusion changes are accompanied by changes in the phase difference between tagged and control images. These phase changes in turn are indicative of arterial volume and/or velocity changes during activation. MP activation is clear in the whole case (Fig. 4i) and similar in the PID case (Fig. 4h) but much reduced in the crush case (Fig. 4g). Although the whole and PID cases may

have benefited from analysis using a complex model, the crush data did not. We attribute this to the increase in phase noise introduced by the crusher gradients (as seen in Fig. 5j and Table 1).

The contrasts of parameter estimates in the MO and PO models were computed along with the model variance to investigate the details underlying the activation maps. These are displayed in Fig. 5, and the same ROI within the visual cortex (outlined by the black box) is examined. The MP coefficient estimates and their contrasts are nearly identical to those for the MO and PO models and are not shown in Fig. 5. In Fig. 5c, the MO model, whole data (i.e., acquired without arterial suppression) produced larger contrast between active versus rest coefficients in the ROI than the flow-crushed data in Fig. 5a and both of these cases yielded a larger contrast than the PID data in Fig. 5b. MO model variance in Fig. 5d-f was similar for the three data types but slightly lower for the crushed data in Fig. 5d. Thus, the pattern of MO activation of whole data in Fig. 4c was larger than flow-crushed in Fig. 4a and PID
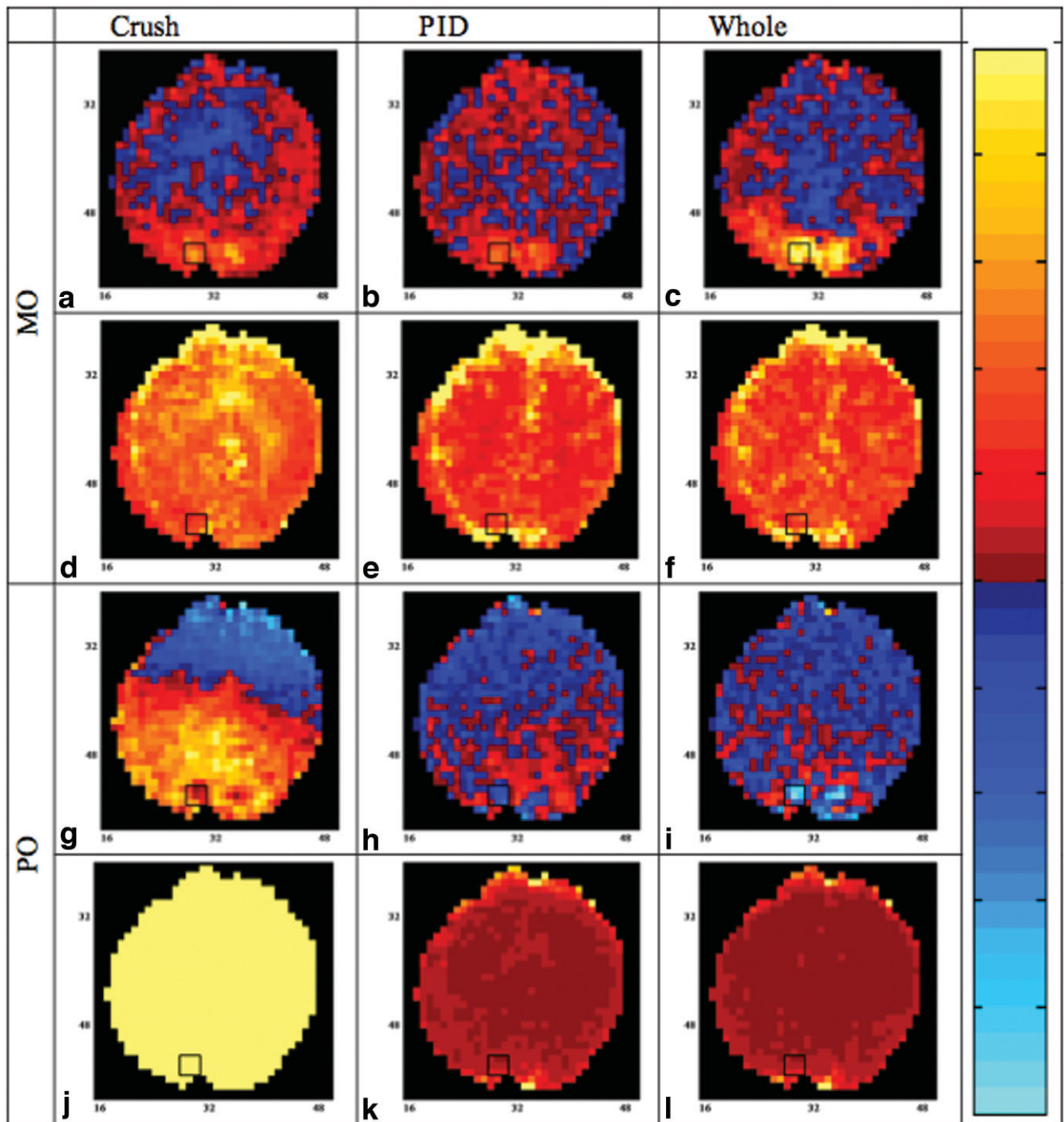
FIG. 5. Maps of the parameter and variance estimates for the magnitude-only and phase-only models. **a-l:** (a) MO crush Cβ, (b) MO PID Cβ, (c) MO whole Cβ, (d) MO crush σ (2), (e) MO PID σ (2), (f) MO whole σ (2), (g) PO crush Dγ, (h) PO PID Dγ, (i) PO whole Dγ, (j) PO σ (2) crush, (k) PO σ (2), PID, (l) PO σ (2) whole. The color-bar maximum values are 35 AU for (a)-(c), 1250 AU (2) for (d)-(g), 0.5 degree for (h)-(j), and 0.05 degree (2) for (k)-(m).

data in Fig. 4a because of differences in the tag versus control contrast coefficients, with little difference in residual model variance in Figs. 5d-f.

In the case of flow-crushed data, the PO model produced a parameter estimate map (Fig. 5g) in which pairs of large, positive clusters could be clearly seen qualitatively at the same location as the active region detected by the MO model (see Fig. 4a, 4b = 4,4, and 4c). In the PID and whole

data in Figs. 5h and 5j = 5,5, the contrast was negative and smaller than in the flow-crushed data. The residual variance of the PO model was much larger for the crush data (Fig. 5j) than for the PID or whole data (Fig. 5k and 5h = 5,5, as previously described). Although a few pixels in the region were statistically detectable by the PO model in the case of PID data, the use of crusher gradients did not yield statistically significant activation by the PO model.

Table 1
Statistics Extracted from the Square ROI in the Visual Cortex*

	Crush			PID			Whole		
	MO	PO	MP	MO	PO	MP	MO	PO	MP
β_0	2470	—	2469	3050	—	3050	3122	—	3122
β_1	−17.17	—	−17.18	8.589	—	8.619	−9.731	—	−9.701
β_2	19.84	—	19.80	24.24	—	24.26	41.43	—	41.44
β_3	36.24	—	36.28	38.47	—	38.48	72.51	—	72.51
$C\beta$	16.40	—	16.48	14.23	—	14.22	31.15	—	31.08
γ_0	—	158.0	158.1	—	127.0	127.0	—	114.4	114.4
γ_1	—	−0.9969	−1.0078	—	−0.3070	−0.3101	—	−0.1785	−0.1797
γ_2	—	−0.1749	−0.1772	—	−0.1078	−0.1082	—	−0.2155	−0.2158
γ_3	—	−0.0388	−0.0402	—	−0.2070	−0.2074	—	−0.5015	−0.5013
$D\gamma$	—	0.1361	0.1371	—	−0.0992	−0.0992	—	−0.2860	−0.2854
σ^2	436.0	3.2483	3234	531.4	0.2542	593.1	532.7	0.2442	593.9
$-\log_{10}(p)$	5.919	.2131	.9017	4.276	.8956	3.671	Inf	6.263	Inf

*Magnitude coefficient values are in AU, magnitude variance values in AU squared, phase coefficient values in degrees, and phase variances in degrees squared.

Some phase difference between rest and activation was detected in the PID data, but it was more prominent in the whole data. The MP coefficient estimates and their contrast were nearly identical to those for the MO and PO models. However, the MP residual variance was much larger for the flow-crushed data than for the PID or whole data because of the large phase variation. This is quantitatively examined with average statistics for the three activation models in the 3 × 3 ROI indicated by the black box in Fig. 5 and displayed in Table 1.

From Table 1, it can be seen that when no significant phase contrast is present, as in the crush data, the MO model performs better than the MP model that detects MP contrast (although the coefficient estimates are similar). In the PID and whole data the MO model performs slightly better than the MP model (although the coefficient estimates are similar). This is due to unmodeled temporal phase variations in the data (most likely of physiologic origin), which increase the residual variance and decrease detection power. Approaches to reduce the phase noise are the subject of future research and are in the Discussion section.

Simulation Study

Fig. 6 displays surfaces for $P = 0.05$ thresholded detection power for the MO, PO, and MP models. In these simulations, the MO model exhibits equivalent CNR detection power regardless of TRPC as seen in Fig. 6a. The PO model exhibits equivalent TRPC contrast detection power regardless of CNR, as seen in Fig. 6b. The MP model exhibits combined CNR and TRPC detection power, as seen in Fig. 6c. When CNR is present and no TRPC is present, the MP model exhibits slightly lower detection power than the MO model, whereas when TRPC is present and no CNR is present, the MP model exhibits slightly lower detection power than the PO model. Hence, the MP model detects MO and/or PO contrast.

DISCUSSION

FMRI data are intrinsically complex valued, although the phase data are routinely discarded. Our simulations sug-

gest that it is possible to improve detection under ideal conditions with the MP model over the MO model by including the phase. The potential improvement with the MP model is due to its ability to detect changes in either the magnitude or the phase of the signal. However, as seen in Fig. 6, when there is only a task-related magnitude change (phase change), a model that is specifically designed to detect only magnitude changes (phase changes) is slightly better than one that is designed to also detect TRPCs (magnitude changes) because of the increase in the dimensionality of the contrast space from adding dimensions that contribute zero signal.

Furthermore, our data indicate that there is a phase difference between control and tagged images in ASL experiments and that this phase difference is related to flow because the phase difference increases with activation and also hypercapnia, a known paradigm that causes systemic increases in blood flow. The ASL data also indicate that the phase difference comes from arterial sources rather than capillary or tissue sources and that removing the arterial contributions reduces the phase differences dramatically. Under ideal conditions, these analyses could render ASL FMRI a more competitive alternative to BOLD FMRI by either increasing the detection power of typical ASL FMRI experiments or, more important, selecting acquisition parameters that will increase the ASL signal (by minimizing the use of postinversion delays or flow-crushing gradients and/or selecting shorter pulse repetition times) and adjusting for larger vascular contributions on the postacquisition data analysis. The current data presented demonstrate a detectable activation signal in the phase of ASL signals. The complex activation model that we are using follows the classic thermal white noise model and does not account for physiologic nonwhite noise in the phase. One approach to reduce its contribution is to include nuisance regressors in the phase design matrix (5). It can be difficult to provide valid regressors for phase, and even when properly modeled, dynamic image warping artifacts still remain, currently making this a less attractive solution (22). However, it has been shown that this phase noise can be significantly decreased to near ideal conditions with the use of a dynamic field mapping method and
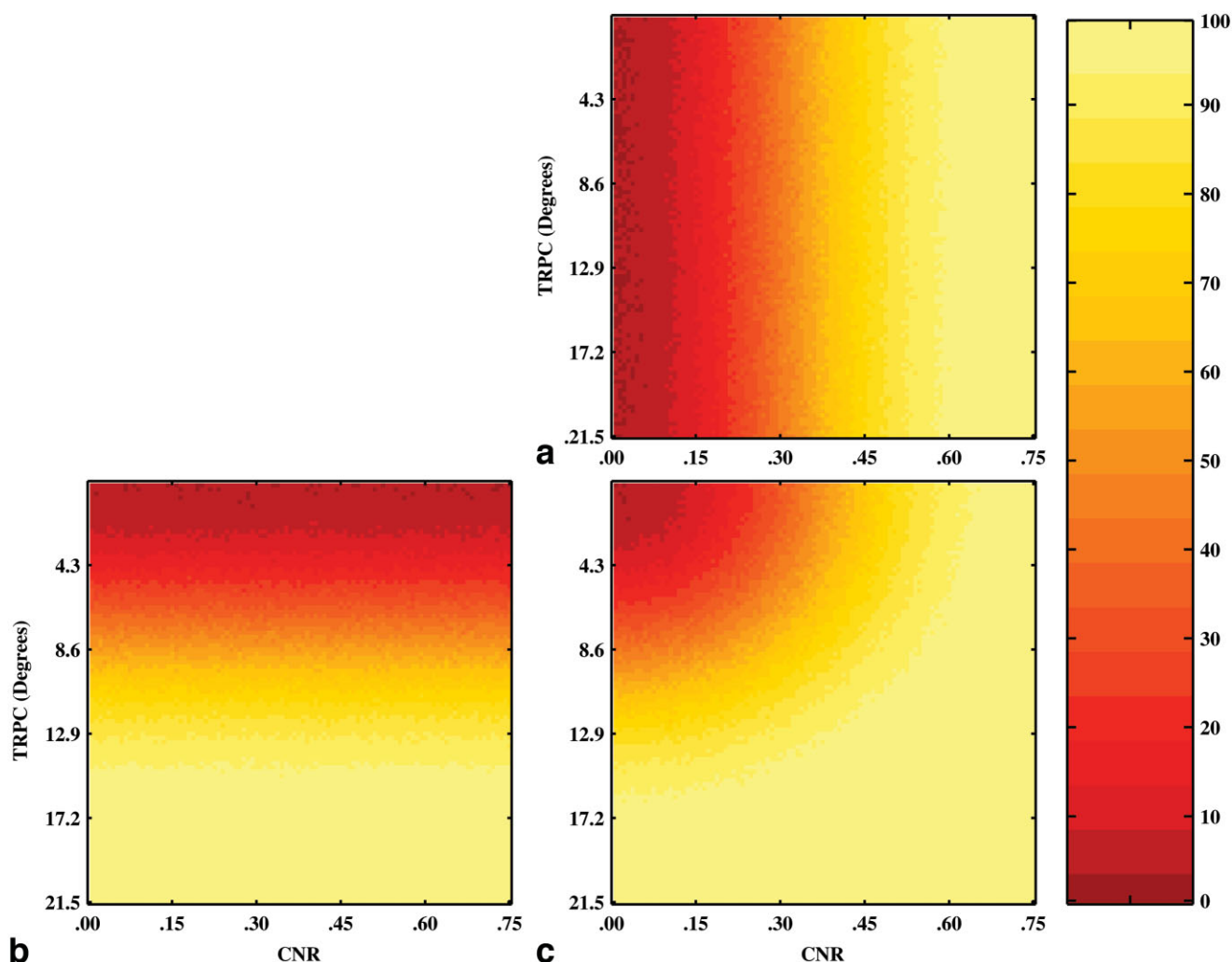
FIG. 6. Power surfaces for *P* = 0.05 thresholded, (a) MO power, (b) PO power, (c) MP power. CNR varies from 0 to 0.75 from left to right in 100 equal steps. TRPC varies from 0 to 0.375 in degrees from top to bottom in 100 equal steps.

that phase-sensitive FMRI analysis methods can be reliably used (22). The dynamic field mapping method (22) was developed for cartesian *k*-space trajectories and needs to be extended to spiral *k*-space trajectories, as used for our data.

These results must be viewed in the context of the vascular anatomy and hemodynamics of the brain. Duong and Kim (24) reported arterial cerebral blood volume of 29% in rats, including the capillary fraction. Cortical surface arteries have been reported to contribute to the cerebral blood volume approximately 15% in cats (25) and 21% in human subjects (26), and their velocity ranges from 10 to 60 cm/s. Penetrating arterioles from the cortical surface into the deeper layer of the cortex have a smaller diameter and run mainly parallel to one another (27); hence, the blood within them flows in a coherent manner. These penetrating arterioles are particularly dense in layers 1 through 4 of the cortex.

In ASL experiments, the venous contributions are negligible because the inversion label relaxes well before reaching the venous compartment. The arterial contribution is routinely treated as contamination of the per-

fusion signal and consequently suppressed by using postinversion delays or flow-crushing gradients (failure to do so results in overestimation of perfusion in quantitative maps). Hence, the observed ASL signal arises from the labeled water within the arterioles and capillaries, as well as those water spins that have exchanged into the tissue.

The use of postinversion delays allows the bulk of the labeled blood to leave the arterial compartment, but a fraction always remains in the arterioles because of the arterial dispersion (18). Flow crushers can also be used to reduce the arterial contribution from the ASL signal, but because arteriolar velocities have been reported to be in the range of 1 cm/s (28), the arteriolar signal is unlikely to be suppressed by them. Instead, flow crushers increase the phase gained in the ASL signal at the arteriolar level. In short, the flow crushers and postinversion delays remove the ASL signal from the larger arteries, but the signal from the smaller penetrating arterioles is preserved. These arteriolar contributions to the arterial cerebral blood volume are small, approximately 3-5% of the cerebral blood volume in humans (29), and are considered part of the blood

supply to the voxel of interest (30) and hence are not considered as part of the arterial contamination.

We observed in the resting state data that the phase difference between control and tagged images decreased dramatically as the arterial signal was removed. In the activation case, subtle changes in the phase difference between control and tagged could be detected by the PO and MP models when the arterial contribution was preserved, but they were much smaller when the arterial contribution was removed by postinversion delays or by crushers.

A potential confound in the correlation analysis is that the SNR of the raw time courses is reduced by the use of flow crushers that null the arterial signal. Reduced SNR would decrease the correlation coefficient of the signals. This is not so much the case with postinversion delays because the arterial signal is preserved in the unsubtracted data, even if the labeled blood has cleared the arteries. It must be noted that although the total ASL signal (the difference between control and tagged images) is reduced by the clearance of the arterial label during the postinversion delay, the label content in the tissue compartment remains unchanged until the arterial compartment clears. The amount of label in the tissue indeed decreases when the postinversion delay exceeds the transit time because tagging time is also reduced, but at a slower rate than that in the arterial compartment (30). Since the magnitude of the subtracted ASL signal was reduced by the crusher gradients and the first postinversion delay (1200 ms) by approximately the same amount (44, 46, and 45%), we can infer that the postinversion delay of 1200 ms accounts mostly for the label clearing the arterial compartment, rather than a reduction of tissue label because of shortened tagging time. On the other hand, the signal reduction of 67% due to the 1800-ms postinversion delay implies that the loss in tissue label could account for the observed reduction of the phase difference.

The use of a pair of flow-crushing gradients dramatically increased the variance of the phase over time, as diffusion gradient pairs are known to do. This increase in phase noise was very detrimental to the PO and MP analyses, essentially yielding no active voxels in the visual cortex.

Including postinversion delays to remove the arterial label's contribution to the signal also reduced the sensitivity to activation-related perfusion changes, but activation could still be detected at lower threshold values because the postinversion delays had no significant effect on the phase noise. We hypothesize that including flow crushers together with the postinversion delays should not change the ASL signal because they both eliminate the arterial compartment. However, we speculate that the phase noise would increase dramatically, as observed in the flow-crushed data.

Activation-induced changes in perfusion are accompanied by changes in blood volume (31) and arterial velocity (32,33). Two-photon bolus injection studies on rats indicated significant changes in transit time from the arteries to the capillaries and venules, but not significant from the arteries to the arterioles (34). It is well known that changes in velocity of blood affect the MR signal's phase, but our data indicate that the arteriolar volume is too small to show large phase changes in the PO analysis. Although the

effect is still observable in the PID data, the number of active voxels is reduced relative to that of the other models because of the large phase noise, as Fig. 5 and Table 1 indicate. However, the MP analysis of the PID and whole data did show significant activation in the visual cortex while reducing the number of active voxels outside the visual cortex, indicating that including the phase information into the model decreased the size of the activation region and led to an apparent increase in the focality of the analysis.

Although absolute quantification of perfusion is not necessary for most cognitive psychology FMRI experiments, it is certainly beneficial. Current perfusion models are based solely on the magnitude of the ASL signal and discard the phase. Although these quantification models may not be fully efficient from a statistical point of view, it must be noted that they are still valid under the model described in Fig. 1 and the phase effects described and reported in the present work. Including phase information in quantification of perfusion from the ASL signal is desirable but not straightforward because blood flow is proportional to the product of both blood velocity and blood volume (assuming no changes in vessel length). Because no large changes in transit time have been reported between arteries and arterioles, the phase of the ASL signal can be seen as an indicator of vascular volume, particularly in the label images. The phase information can be used to estimate velocity along the images vascular volume and/or to differentiate the velocity contribution to the increases in cerebral blood flow. This might be advantageous, considering some of the current methods to measure cerebral blood volume and mean transit time. For example, dynamic susceptibility contrast bolus-injection experiments quantify perfusion as cerebral blood volume over the mean transit time through the capillary. However, a robust implementation of velocity estimates would require encoding velocity in all cardinal directions. More problematic is that this calculation is likely to be confounded by multiple vessels with different orientations within a voxel. Thus, a more complete model that includes the phase of the signal to efficiently use all the information available is beyond the scope of this work but currently under investigation.

Finally, although preserving the whole arterial signal (by not using flow crushers or postinversion delays) prevents the classic quantification of perfusion, it enhances the ability to detect neuronal activity. Thus, when designing an ASL-based FMRI experiment, investigators should consider whether their main goal is to detect or quantity changes in blood flow. In experiments in which CNR is low, it may be useful (or even necessary) to sacrifice quantification for the sake of sensitivity. For example, a multi-session study in which BOLD imaging is problematic because of scanner drifts would still benefit from nonquantitative ASL techniques. Although outside the scope of the present work, ASL techniques that leverage transit time changes to amplify activation responses (35,36) should also benefit from complex-valued analysis.

In summary, there is valuable phase information in the phase of ASL-based FMRI time series that could be used to increase activation if modeled properly. The complex activation model that we are using follows the classic thermal noise model and does not account for physiologic

noise in the phase. The source of this phase information is arterial in nature. Because there is arteriolar signal still present even after arterial suppression, the phase information is greatly reduced but still detectable in some of the pixels of the active region (see Fig. 4). One must keep in mind, though, that if arterial suppression is achieved through diffusion crushers, the phase noise overwhelms the signal. Thus, postinversion delays are a preferable method of suppression when analyzing the phase of ASL images.

APPENDIX

MO, PO, and Magnitude-Phase Activation Models

Here, we describe the activation models that are necessary for the maximum likelihood estimation process. These three models can be described from a complex-valued perspective. Let the complex-valued measurement in a voxel $y_{Rt} + iy_{It}$ at time t be described as

$$\begin{pmatrix} Y_{Rt} \\ Y_{It} \end{pmatrix} = \begin{pmatrix} \rho_t\cos\theta_t \\ \rho_t\sin\theta_t \end{pmatrix} + \begin{pmatrix} \eta_{Rt} \\ \eta_{It} \end{pmatrix}, \qquad [A1]$$

where ρ_t and θ_t are the true MP while η_{Rt} and η_{It} are additive statistically independent normally distributed noise with zero mean and variance σ (2). From Eq. [A1], a joint distribution $p(y_{Rt}, y_{It}|\rho_t, \theta_t, \sigma (2))$ and likelihood can be presented. This distribution can be converted to MP polar coordinates

$$p(m_t, \varphi_t|\rho_t, \theta_t, \sigma^2)$$

$$= \frac{m_t}{2\pi\sigma^2}\exp\left\{-\frac{1}{2\sigma^2}[m_t^2 + \rho_t^2 - 2\rho_1 m_t\cos(\varphi_t - \theta_t)]\right\}$$

$$[A2]$$

Upon discarding the phase portion of the data (equivalent to marginalizing Eq. [A2] with respect to φ_t), the observed magnitude m_t follows the Ricean distribution

$$p(m_t|\rho_t, \sigma^2)$$

$$= \frac{m_t}{\sigma^2}\exp\left\{-\frac{m_t^2 + \sigma_t^2}{2\sigma^2}\right\} \int_{\varphi_t = -1}^{1} \frac{1}{2^1}\exp\left\{\frac{\rho_t m_t}{\sigma^2}\cos(\varphi_t - \sigma_t)\right\}d\varphi_t$$

$$[A3]$$

as has been previously described (2-4). The true underlying magnitude in Eq. [A3] is then modeled as $m_t = x_t'\beta = \beta_0 + \beta_1 x_{1t} + \cdots + \beta_{q1}x_{q1t}$ where x_t' is the tth row of a magnitude design matrix X and β is a $q_1 + 1$ dimensional vector of magnitude regression coefficients. This Ricean distribution is well approximated by the normal distribution with mean ρ_t and variance σ (2) when the temporal SNR is high, above 7.5 (3). The usual MO linear regression model $m_t = x_t'\beta + \varepsilon_t$, parameter estimates, and test statistics follow where ϵ_t are additive, statistically independent, normally distributed noise with zero mean and variance σ (2) (3).

Upon discarding the magnitude portion of the data (equivalent to marginalizing Eq. [A2] with respect to m_t), the observed phase φ_t follows the distribution

$$p(\varphi_t|\rho_t, \theta_t, \sigma^2) = \frac{1}{2^1}\exp\left\{-\frac{\rho_t^2}{2\sigma^2}\right\}$$

$$\times\left[1 + \frac{\rho_t\sqrt{2^1}}{\sigma}\cos(\varphi_t - \theta_t)\exp\left\{\frac{\rho_t^2\cos(\varphi_t - \theta_t)}{2\sigma^2}\right\}\right.$$

$$\left.\Phi\left(\frac{\rho_t^2\cos(\varphi_t - \theta_t)}{\pi}\right)\right] \quad [A4]$$

as has been previously described (2,4). The true underlying phase in Eq. [A4] is then modeled as $\theta_t = X_t'\gamma = \gamma_0 + \gamma_1 x_{1t} + \cdots + \gamma_{q2}X_{q2t}$ where γ is a $q_2 + 1$ dimensional vector of phase regression coefficients. We use the same design matrix in MP, although this is not required (5,6). This distribution is well approximated by the normal distribution with mean θ_t and variance (σ/ρ_t) (2) when the temporal SNR is reasonable (19). The usual PO linear regression model $\varphi_t = x_t'\beta + \delta_t$, parameter estimates, and test statistics follow where δ_t are additive statistically independent normally distributed noise with zero mean and variance (σ/ρ_t) (2) (19).

Alternatively, the MP can be modeled simultaneously as $\rho_t = x_t'\beta = \beta_0 + \beta_1 x_{1t} + \cdots + \beta_{q1}x_{q1t}$ and $\theta_t = x_t'\gamma = \gamma_0 + \gamma_1 x_{1t} + \cdots + \gamma_{q2}X_{q2t}$ from Eq. [A1] and Eq. [A2]. Upon doing so, a likelihood can be formed from Eq. [A2], maximized under null and alternative hypotheses, and a likelihood ratio statistic formed (5,6).

REFERENCES

1. Rowe DB, Logan BR. A complex way to compute fMRI activation. Neuroimage 2004;23:1078–1092.
2. Rowe DB. Modeling both the magnitude and phase of complex-valued fMRI data. Neuroimage 2005;25:1310–1324.
3. Menon RS. Postacquisition suppression of large-vessel BOLD signals in high-resolution fMRI. Magn Reson Med 2002;47:1–9.
4. Nencka AS, Rowe DB. Reducing the unwanted draining vein BOLD contribution in fMRI with statistical post-processing methods. Neuroimage 2007;37:177–188.
5. Liu T, Wong E. A signal processing model for arterial spin labeling functional MRI. Neuroimage 2005;24 :207–215.
6. Mumford JA, Hernandez-Garcia L, Lee GR, Nichols TE. Estimation efficiency and statistical power in arterial spin labeling fMRI. Neuroimage 2006;33:103–114.
7. Wong E, Buxton R, Frank L. Implementation of quantitative perfusion imaging techniques for functional brain mapping using pulsed arterial spin labeling. NMR Biomed 1997;10:237–249.
8. Noam H, Ugurbil K, Uludag K, Yacoub E. Frontiers of brain mapping using MRI. J Magn Reson Imaging 2006;23:945–957.
9. Pandey K, Noll D. Characterization and correction of artifacts from dynamic interaction between motion and position dependent off-resonance patterns. In: Proc ISMRM, 2008; Toronto, ON. p 3121.
10. Perthen JE, Bydder M, Restom K, Liu TT. SNR and functional sensitivity of BOLD and perfusion-based fMRI using arterial spin labeling with spiral SENSE at 3 T. Magn Reson Imaging 2008;26:513–522.
11. Yang Y, Gu H, Stein AE. Simultaneous MRI acquisition of blood volume, blood flow, and blood oxygenation information during brain activation. Magn Reson Med 2004;52:1407–1417.

12. Le Bihan D, Breton E, Lallemand D, Grenier P, Cabanis E, Laval-Jeantet M. MR imaging of intravoxel incoherent motions: application to diffusion and perfusion in neurologic disorders. Radiology 1986;161:401–407.

13. Haacke EM, Lenz GW. Improving MR image quality in the presence of motion by using rephasing gradients. AJR Am J Roentgenol 1987;148: 1251–1258.

14. Dumoulin CL. Phase contrast MR angiography techniques. Magn Reson Imaging Clin N Am 1995;3:399–411.

15. Hernandez-Garcia L, Lewis D, Moffat B, Branch C. Magnetization transfer effects on the efficiency of flow-driven adiabatic fast passage inversion of arterial blood. NMR Biomed 2007;20:733–742.

16. Garcia D, de Bazelaire C, Alsop D. Pseudo-continuous flow driven adiabatic inversion for arterial spin labeling. In: Proc. ISMRM, 2005; Miami, FLA. p 37.

17. Wu WC, Fernandez-Seara M, Detre JA, Wehrli FW, Wang J. A theoretical and experimental investigation of the tagging efficiency of pseudo-continuous arterial spin labeling. Magn Reson Med 2007;58:1020–1027.

18. Alsop D, Detre J. Reduced transit-time sensitivity in noninvasive magnetic resonance imaging of human cerebral blood flow. J Cereb Blood Flow Metab 1996;16:1236–1249.

19. Vazquez AL, Lee GR, Hernandez-Garcia L, Noll DC. Application of selective saturation to image the dynamics of arterial blood flow during brain activation using magnetic resonance imaging. Magn Reson Med 2006;55:816–825.

20. Rowe DB, Logan BR. Complex fMRI analysis with unrestricted phase is equivalent to a magnitude-only model. Neuroimage 2005;24:603–606.

21. Bandettini PA, Jesmanowicz A, Wong EC, Hyde JS. Processing strategies for time-course data sets in functional MRI of the human brain. Magn Reson Med 1993;30:161–173.

22. Rowe DB, Meller CP, Hoffmann RG. Characterizing phase-only fMRI data with an angular regression model. J Neurosci Methods 2007;161: 331–341.

23. Rowe DB, Hernandez-Garcia L, Lee GR. Complex analysis of ASL fMRI data yields more focal activation. In: Proc. ISMRM 2007; Berlin, Germany. p 1422.

24. Duong TQ, Kim SG. In vivo MR measurements of regional arterial and venous blood volume fractions in intact rat brain. Magn Reson Med 2000;43:393–402.

25. Tomita M, Gotoh F, Amano T, Tanahashi N, Kobari M, Shinohara T, Mihara B. Transfer function through regional cerebral cortex evaluated by a photoelectric method. Am J Physiol 1983;245:H385–398.

26. Leenders KL, Perani D, Lammertsma AA, Heather JD, Buckingham P, Healy MJ, Gibbs JM, Wise RJ, Hatazawa J, Herold S, et al. Cerebral blood flow, blood volume and oxygen utilization. Normal values and effect of age. Brain 1990;113(pt 1):27–47.

27. Duvernoy HM, Delon S, Vannson JL. Cortical blood vessels of the human brain. Brain Res Bull 1981;7:519–579.

28. Nishimura N, Schaffer CB, Friedman B, Lyden PD, Kleinfeld D. Penetrating arterioles are a bottleneck in the perfusion of neocortex. Proc Natl Acad Sci U S A 2007;104:365–370.

29. Berne RM, Levy MN. Cardiovascular physiology. St. Louis, MO: Mosby-Year Book; 1992. pp vi, 298.

30. Buxton RB. Introduction to functional magnetic resonance imaging: principles and techniques. Cambridge, UK: Cambridge University Press; 2002. pp xi, 523.

31. Grubb RL Jr, Raichle ME, Eichling JO, Ter-Pogossian MM. The effects of changes in $PaCO_2$ on cerebral blood volume, blood flow, and vascular mean transit time. Stroke 1974;5:630–639.

32. Lee G, Hernandez-Garcia L, Noll D. Effects of activation induced transit time changes on functional turbo ASL imaging. In: Proc. ISMRM P 2004; Kyoto, Japan. p 519.

33. Gonzalez ATJ, Alsop D, Detre J. Cerebral perfusion and arterial transit time changes during task activation determined with continuous arterial spin labeling. Magn Reson Med 2000;43:739–746.

34. Hutchinson EB, Stefanovic B, Koretsky AP, Silva AC. Spatial flow-volume dissociation of the cerebral microcirculatory response to mild hypercapnia. Neuroimage 2006;32:520–530.

35. Hernandez-Garcia L, Lee GR, Vazquez AL, Noll DC. Fast, pseudo-continuous arterial spin labeling for functional imaging using a two-coil system. Magn Reson Med 2004;51:577–585.

36. Hernandez-Garcia L, Lee GR, Vazquez AL, Yip CY, Noll DC. Quantification of perfusion fMRI using a numerical model of arterial spin labeling that accounts for dynamic transit time effects. Magn Reson Med 2005;54:955–964.